NEAR-INFRARED OBSERVATIONS OF OUTFLOWS AND YOUNG STELLAR OBJECTS IN THE MASSIVE STAR-FORMING REGION AFGL 5180

S. Crowe[1], R. Fedriani[2], J.C. Tan[1,3], M. Whittle[1]

[1] Department of Astronomy, University of Virginia, Charlottesville, Virginia 22904, USA

[2] Instituto de Astrofísica de Andalucía, CSIC, Glorieta de la Astronomía s/n, 18008 Granada, Spain

[3] Department of Space, Earth & Environment, Chalmers University of Technology, 412 93 Gothenburg, Sweden

ABSTRACT

Massive stars are significant throughout the universe, as they impact their surroundings from the early stages of their formation until they die in the form of supernova. Observations in the near-infrared (NIR) of the bright and large-scale (~pc) jets which young stars ubiquitously produce during their formation process can place important constraints on the phenomenon of massive star formation. Here, I present a detailed NIR view of the massive star-forming region AFGL 5180 utilizing imaging from the Large Binocular Telescope (LBT) with both seeing-limited and extremely high-resolution (~90 milli-arcsecond) Adaptive Optics data, as well as imaging from the Hubble Space Telescope (HST). This unprecedented view into the AFGL 5180 complex reveals highly clustered star formation, evidenced by the presence of several multidirectional outflows and confirmed by the detection of over a dozen compact sub-millimeter sources using data from the Atacama Large Millimeter/Submillimeter Array (ALMA). High stellar densities in the vicinity of the central massive (~12 Msun) protostar agree favorably with recent numerical simulations and indicate that low- and high-mass star formation is occurring in AFGL 5180 in a crowded manner, shedding light on the process of star formation.

1. Introduction

Massive stars play a significant role throughout the Universe, especially via the regulation of the physical and chemical evolution of galaxies that ultimately influences all star and planet formation activity in these systems. However, the formation mechanism of massive stars remains actively debated, especially between core accretion models, i.e., scaled-up versions of low-mass star formation theory (e.g., McKee & Tan 2003), and competitive accretion models (e.g., Bonnell et al. 2001; Wang et al. 2010; Grudic et al. 2022; see, e.g., Tan et al. 2014 for a review). Detailed high-resolution infrared observational studies of regions of massive star formation, where individual sources can be resolved and characterized, are needed to test theoretical models.

Here, we present NIR observations of the massive star-forming region AFGL 5180, also known as IRAS 06058+2138 or G188.949+0.915 (peak pixel in our near-infrared image: RA(J2000) = 06:08:53.38, Dec(J2000) = +21:38:28.38; see Sect. 2). Previous studies have noted the presence of a prominent east-west ^{12}CO outflow in the region, with a blue-shifted lobe to the east and a red-shifted lobe to the west (Snell et al. 1988). Tamura et al. (1991) and Hodapp (1994) also noted the high level of nebulosity associated with the source, particularly in the infrared. Tofani et al. (1995) reported detection of several water masers towards the region, clustering both towards the main nebulosity and towards the south of it, providing evidence for two main sites of star formation. Davis et al. (1998) identified multiple knots of shocked molecular hydrogen emission, suggesting the presence of multiple outflows. Tamura et al. (1991) identified a separate NW-SE outflow using NIR K-band polarization maps, and Yao et al. (2000) associated this outflow with an embedded source identified through NIR polarimetric lines. Longmore et al. (2006) identified six sources in the mid-infrared (MIR) which they associated with star formation activity. Mutie et al. (2021) used archival ALMA Band 6 and 7 data to identify gas cores associated with YSO candidates, finding 8 cores in the region, MM1–8, of which one, MM1, appears to be associated with massive star formation activity.

The structure of our paper is as follows. We present the observations and data reduction used in this study in Sect. 2. Results and characterization of the region are presented in Sect. 3. A summary and conclusion are given in Sect. 4.

2. Observations and Data Reduction

2.1 Large Binocular Telescope

Observations were taken on 10 October 2020 with the Large Binocular Telescope (LBT) in binocular mode, i.e. utilizing both mirrors simultaneously, with the LBT Utility Camera in the Infrared (LUCI; Seifert et al. 2003) instrument in seeing limited mode (UV-2020B-04; PI: J. C. Tan). The N3.75 camera with a pixel scale of 0.12″and FOV of 4′ × 4′ was used. The filters K and Brγ, which are centered at the wavelengths 2.194 and 2.170 μm, respectively, were employed on the LUCI1 instrument mounted on the left (SX) mirror, and the filters K and H2, which are centered at the wavelengths 2.194 and 2.124 μm, respectively, were employed on the LUCI2 instrument mounted on the right (DX) mirror. The central coordinates of the image are RA(J2000) = 06:08:53.60, Dec(J2000) = +21:38:15.61. The images have a position angle (PA) of 0°.

Observations were also taken on 3 November 2020 with the LUCI-1 instrument (see previous paragraph) in the adaptive optics (AO) assisted mode with the Single conjugated adaptive Optics Upgrade for the LBT (SOUL; Pinna et al. 2016) as part of the SOUL Commissioning Science Run scheduled for 1–6 November 2020 (UV-2020B-501; PI: J. C. Tan). The N30 camera with a pixel scale of 0.015″and FOV of 30″ × 30″ was used. The filters K, H2, and Brγ which are centered at the wavelengths 2.194, 2.124, 2.170 μm, respectively, were employed on the LUCI-1 instrument mounted on the left (SX) mirror. The central coordinates of the image were RA(J2000) = 06:08:54.042, Dec(J2000) = +21:38:26.920. The AO guide star used, 082-000146 (RA(J2000) = 06:08:54.271, Dec(J2000) = +21:38:24.324, R = 15.41 mag), was located at 4.2″ from the center of the image. The images were taken with a PA of 150◦, though the final images used for analysis were rotated to a PA = 0◦.

The data were reduced with custom python scripts using the python packages ccdproc (Craig et al. 2022), astropy (Astropy Collaboration 2022) and photutils (Bradley 2023) in the standard way, i.e. via subtraction of sky frames and flat field correction. The images were registered to one another and astrometrically calibrated by matching stars to the images from Hubble Space Telescope (HST), see Sect. 2.2, with an estimated residual of 0.13″ for the seeing-limited images and 0.02″ for the AO images. The Strehl ratio of the AO images were 0.15. The angular resolution of the seeing-limited and AO images were ~0.5″ and ~0.09″, respectively, derived by determining the Full Width at Half Maximum (FWHM) of Moffat profiles of isolated sources identified in each of the images (see Appendix A of Fedriani et al. 2023a, for the details).

2.2. Hubble Space Telescope

Observations were taken with the HST on 13 February 2016 (program ID: 14465; PI: J. C. Tan). The Wide Field Camera 3 (WFC3) instrument was used with a pixel scale of 0.13″and FOV of 2′ × 2′. The filters F110W (J-band), F128N (Paβ), F160W (H-band), and F164N ([FeII]), which have the mean wavelengths 1.180, 1.284, 1.544, and 1.645 μm, and therefore diffraction-limited angular resolutions of 0.12″, 0.13″, 0.16″, and 0.17″, respectively, were employed. The data was downloaded from the Mikulski Archive for Space Science (MAST) as a Hubble Advanced Product (HAP), which are reduced and calibrated using the standard pipeline. The images were astrometrically corrected by matching stars to the Gaia DR3 catalog (Gaia Collaboration 2023), with an estimated residual of 0.0323″, determined by measuring the mean separation between isolated sources identified using the algorithm DAOFIND (Stetson 1987) and their Gaia counterparts. The final drizzle images have a postion angle (PA) of 0◦.

2.3. Atacama Large Millimeter/submillimeter Array

We also used Atacama Large Millimeter/Submillimeter Array (ALMA) 1.3 mm (Band 6) and 0.9 mm (Band 7) continuum data. The ALMA Band 6 observations were carried out on 23 April 2016 with the C36-3 configuration, and on 8 September 2016 with the C36-6 configuration (ALMA project ID: 2015.1.01454.S, PI: Y. Zhang). The total integration times were 3.5 and 6.5 min in the two configurations, respectively. Forty-one antennas were used with baselines ranging from 15–462 m in the C36-3 configuration, and 38 antennas were used with baselines ranging from 15 m to 3.2 km in the C36-6 configuration. J0750+1231 and J0510+1800

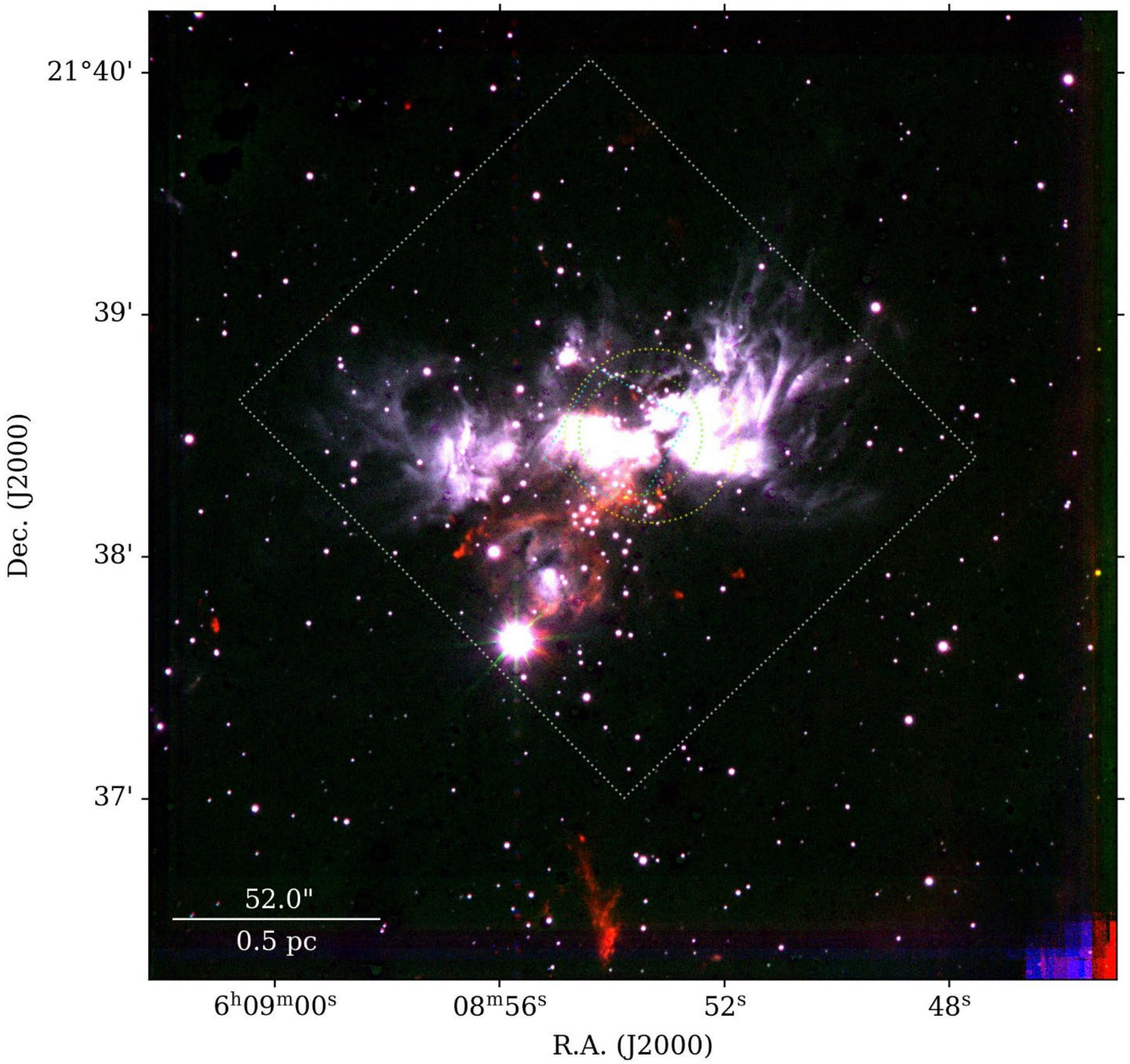

Figure 1: RGB image of the AFGL 5180 complex in LBT seeing-limited data. The white box represents the FOV of the HST data; the blue box represents the AO data FOV; the green and yellow circles represent the ALMA Bands 7 and 6 FOVs, respectively.

were used for bandpass calibration and flux calibration. J0603+2159 was used as a phase calibrator. The ALMA Band 7 observations were carried out on 2 December 2017 using the C43-7 configuration with 48 antennas and baselines ranging from 41.4 m to 6.9 km (ALMA project ID: 2017.1.00178.S, PI: T. Hirota). The total integration time was 10 min. J0510+1800 was used for bandpass calibration and flux calibration and J0613+2604 was used as a phase calibrator.

3. Results

NIR Imaging of the AFGL 5180 Complex

Figure 1 shows an RGB image of the fullest extent of the AFGL 5180 complex covered by the LBT seeing-limited data (4′ × 4′); red is used for the H2 filter, green for K, and blue for

Brγ. Readily apparent is the prominent east-west outflow, which is captured in all three LBT LUCI filters used; however, the narrow-band H2 image reveals a large number of additional features, including an extended emission protruding from the main complex to the southeast, as well as several additional knots, particularly the bright bow shock to the south, extending over several arcminutes from the central region. These numerous H2 knots, which appear to emanate in a wide variety of directions away from the central region, provide evidence of multiple outflows in the complex.

Figure 2: RGB image of the inner portion of the AFGL 5180 complex in LBT AO data.

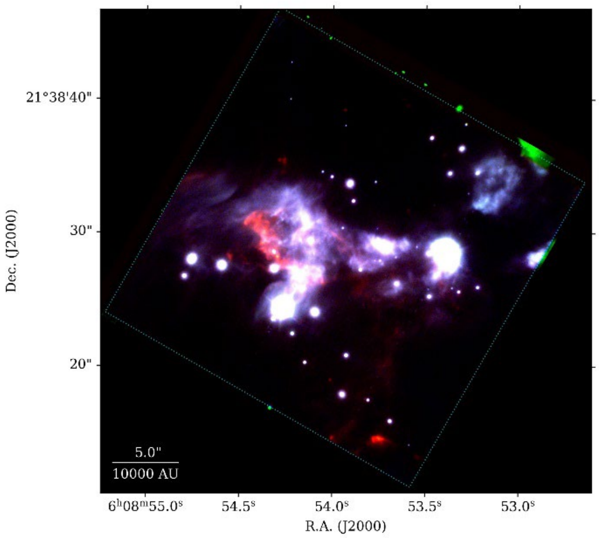

Figure 2 shows an RGB image, with the same color scheme as the previous image, of the inner outflowing region of AFGL 5180 as seen with LUCI-1 SOUL AO, in particular capturing in high resolution the eastern blue-shifted jet. The emission in the NIR has a cone-like morphology, although the complex structure makes it difficult to determine a precise value of the opening angle of the cone. Nevertheless, the cone appears to trace directly back to a source located near the bright emission on the right in the image, however this driving protostar may be obscured in the NIR image. As in the seeing-limited image, a number of prominent H2 features are seen, both within the main cone and also in more widespread locations, e.g., to the S and NE, suggesting the possibility of multiple outflow driving sources in the region.

Figure 3 shows an RGBC image from the HST of the AFGL 5180 complex. Here red is used for F164N, green is used for F160W, blue is used for F110W, and cyan is used for F128N. The prominent east-west outflow is again clearly seen, with a few [FeII] knots contained within the eastern jet and a large reflection nebula to the west. A few [FeII] knots can also be seen to the N, W, and S, which are noticeably off-axis with respect to the main outflow, corroborating the LBT LUCI H2 data and again indicating the presence of multiple driving sources.

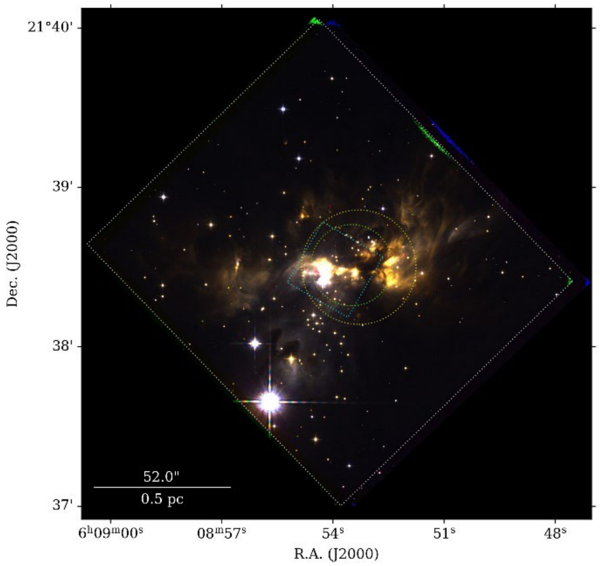

Figure 3: RGB image of the AFGL 5180 complex in HST data.

Characterization of the AFGL 5180 Complex

The sub-mm population in AFGL 5180

Mutie et al. (2021) provide an analysis of ALMA Band 6 data towards AFGL 5180, from which they identify at least 8 dust cores, called MM1−8, among which MM1 and MM2 are found to have corresponding compact sources seen in the Band 7 high resolution image. However, some of the cores identified from the ALMA Band 6 data, such as MM3 and MM4, appear as rather diffuse emission unlike the compact morphology which would be expected of a protostar (see Figs. 6 and 5 of Mutie et al. 2021). Furthermore, inspection of the Band 7 data reveals many additional compact continuum sources which are unidentified in Mutie et al. (2021). For these reasons, we present a re-analysis of the ALMA Band 6 and 7 data, for which we have re-reduced the data.

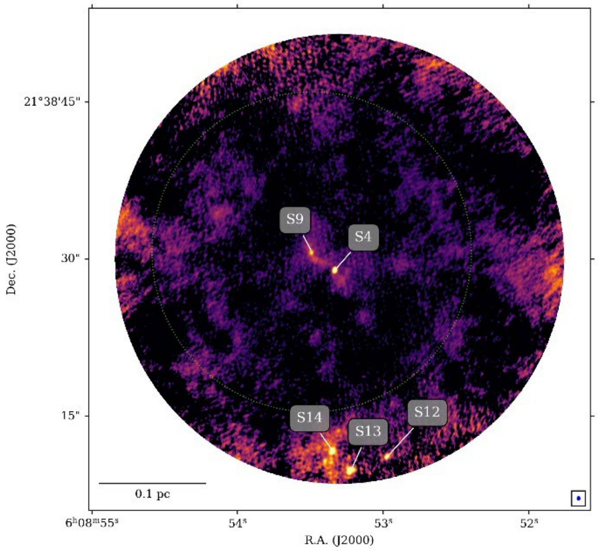

Figure 4: ALMA Band 6 image of the mm cores in the AFGL 5180 complex.

From the high-resolution Band 7 data, we identify 12 compact continuum sources within 15″ from the center, which are readily apparent upon visual inspection (see Fig. 5 and Table 1). Among these sources, S4 and S9a/S9b are reported by Mutie et al. (2021) but labeled as MM1 and MM2, respectively. The other sources are newly identified. Due to the smaller FOV of the Band 7 image, the southern cores seen in the Band 6 image are not covered by the Band 7 image. Therefore, we supplement the source list with these three cores, S12–14 (labeled MM6–8 in Mutie et al. 2021). However, it is unclear how many compact sources (YSOs) are really harbored in these cores due to the lack of high-resolution observations in these regions. The coordinates of each source are obtained with 2D Gaussian fitting, and the fluxes are determined from primary beam corrected images by integrating the flux within the fitted Gaussian ellipse at 1.5 × FWHM. This method primarily retrieves flux from the central compact structure of each source; therefore, the fluxes and masses presented likely represent those of the disk or inner envelope of the sources, rather than the full envelope mass. The properties of each of these sources are summarized in Table 1.

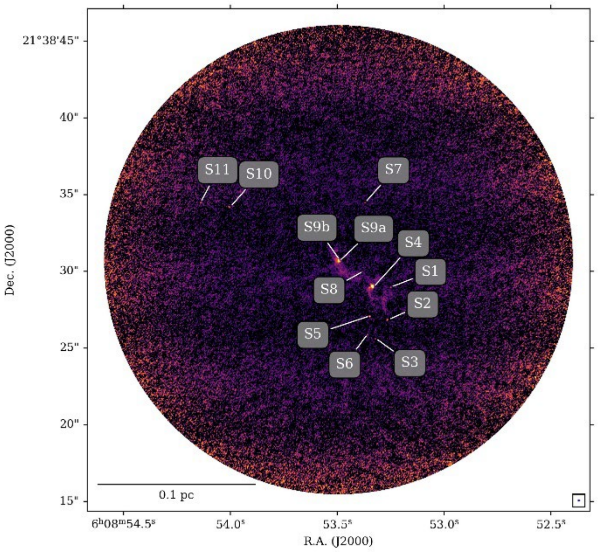

Figure 5: ALMA Band 7 image of the mm cores in the AFGL 5180 complex.

Looking at the distribution of the sources, the sources appear to comprise two main clusters: one containing S1–6, 8, and 9 (hereafter AFGL 5180 M) and another ~15″ (0.15 pc) to the south of AFGL 5180 M containing S12–14 (hereafter AFGL 5180 S). In addition, there are a few other sources (S7, S10 and S11) distributed to the N and NE (see Fig. 5). Both AFGL 5180 M and S appear to be sites of active star formation, based on the presence of multiple water masers (see, e.g., Tofani et al. 1995) and dozens of jet knots. We conclude that these young clusters likely contain many of the

Table 2: Table of Jet knot features identified in the NIR imaging of AFGL 5180.

driving sources responsible for the jet knots observed in the NIR.

Jet Features in AFGL 5180

Jet knots in the AFGL 5180 complex were identified using the H2 and [FeII] continuum-subtracted images, which trace shocked emission from protostellar jets. The Brγ and Paβ continuum subtracted images were also examined but did not have any identifiable compact knot-like features.

Table 1: Millimeter cores observed in AFGL 5180 in the ALMA Bands 6 & 7 data. Associated source names are given from Mutie et al. (2021).

Source name	Associated source	RA(J2000) (J2000)	Dec(J2000) (J2000)	S_6 (mJy)	S_7 (mJy)	M_{mm} $(M_\odot)$	Area (arcsec^2)	S/N
S1	···	06:08:53.25	21:38:28.95	···	1.8	0.017	0.010	11
S2	···	06:08:53.26	21:38:26.83	···	4.2	0.040	0.018	17
S3	···	06:08:53.32	21:38:25.59	···	1.2	0.012	0.011	8
S4	(†)MM1	06:08:53.33	21:38:29.01	51.7	102.6	0.97 | 1.9	0.012 | 0.156	600 | 200
S5	···	06:08:53.35	21:38:27.06	···	4.6	0.044	0.012	25
S6	···	06:08:53.36	21:38:25.86	···	1.8	0.017	0.012	8
S7	···	06:08:53.37	21:38:34.46	···	1.3	0.012	0.009	8
S8	···	06:08:53.38	21:38:29.97	···	0.6	0.0059	0.006	5
S9a	(‡)MM2	06:08:53.49	21:38:30.65	18.8	13.6	0.13 | 0.68	0.018 | 0.278	45 | 40
S9b	(‡)MM2	06:08:53.49	21:38:30.72	18.8	9.4	0.089 | 0.68	0.016 | 0.278	40 | 40
S10	···	06:08:54.00	21:38:34.19	···	3.6	0.034	0.016	14
S11	···	06:08:54.14	21:38:34.47	···	2.8	0.026	0.013	11
S12	MM8	06:08:52.97	21:38:11.14	24.0	–	0.71	0.313	11
S13	MM7	06:08:53.22	21:38:09.84	49.4	–	1.5	0.534	14
S14	MM6	06:08:53.35	21:38:11.69	61.3	–	1.8	0.689	11

Knots are identified as extended emission features in the continuum-subtracted images. Their peak intensity is determined in relation to the local standard deviation sampled in the vicinity of the knot candidate. The minimum size of a knot candidate in each image is determined by the angular resolution of the image.

The minimum intensity peak for knot identification in the H2 (seeing-limited and AO) images was set at 3σ, based on the σ level of the dimmest knots apparent in the seeing-limited images, knots 1 and 3. Likewise, the minimum intensity peak for knot identification in the [FeII] image was set at 5σ, based on the σ level of the dimmest knot apparent in the image, knot 13. Table 2 presents a list of all identified knots in the images. Precise coordinates presented in Table 2 were determined via 2D Gaussian fitting of each knot, and Table 2 also provides a prediction of the potential driving core(s) for each knot, and therefore its position angle (relative to N is up for PA = 0◦), and angular separation.

It is worth noting that many of the knots extending away from the main outflowing structure in AFGL 5180 appear to group towards the southeast (see Fig. 1). This morphology can be explained if this side of the outflow forms the near-facing cavity, in which case the jet knots would be expected to be blue-shifted. If the main protostar is forming via core accretion, then the opposite, far-facing cavity is expected to be present and also include jet knots. However, these would likely suffer from higher levels of extinction and thus appear dimmer and be harder to detect. The prediction of blue-shifted knots in the SE group requires confirmation via spectroscopic observations.

YSO Surface Number Density Analysis

Feature	RA(J2000) (J2000)	Dec(J2000) (J2000)	H_2 (σ)	H_2 AO (σ)	[FeII] (σ)	Core(s)	PA (°)	Sep. ($''$)
K1	06:08:51.71	21:37:55.60	5	–	···	S	236	25
K2	06:08:52.09	21:38:34.75	30	–	65	M	288	18
K3	06:08:52.14	21:36:20.69	3	–	–	S	188	110
K4	06:08:52.38	21:38:35.74	25	–	···	M	297	15
K5	06:08:52.80	21:37:50.53	5	–	···	S	197	20
K6	06:08:52.99	21:38:10.57	···	–	8	S	283	3
K7	06:08:53.15	21:38:15.85	19	–	···	S	351	6
K8	06:08:53.16	21:38:12.42	5	–	···	S	343	3
K9	06:08:53.59	21:38:31.67	···	3	···	M	54	5
K10	06:08:53.74	21:38:14.68	56	38	···	S	56	9
K11	06:08:53.93	21:38:39.20	···	5	···	M	40	13
K12	06:08:53.95	21:38:14.83	13	9	···	S	64	11
K13	06:08:54.01	21:38:18.99	···	5	5	M | S	137 | 50	14 | 14
K14A	06:08:54.02	21:36:26.84	21	–	–	M | S	176 | 174	123 | 104
K14B	06:08:54.04	21:36:24.78	19	–	–	M | S	176 | 174	125 | 106
K14C	06:08:54.53	21:36:50.22	11	–	–	M | S	170 | 167	100 | 82
K15A	06:08:54.06	21:38:53.06	···	–	29	M | 13 | 14	23 | 3 | 357	26 | 19 | 19
K15B	06:08:54.06	21:38:50.76	···	–	11	M | 13 | 14	25 | 3 | 356	24 | 17 | 16
K15C	06:08:54.15	21:38:49.85	···	–	8	M | 13 | 14	29 | 8 | 1	24 | 16 | 15
K16A	06:08:54.18	21:38:27.93	···	···	500	3	95	12
K16B	06:08:54.21	21:38:28.47	···	···	590	3	92	12
K16C	06:08:54.23	21:38:27.45	···	15	···	3	97	13
K16D	06:08:54.29	21:38:28.20	···	55	···	3	93	13
K16E	06:08:54.31	21:38:28.47	···	40	···	3	92	14
K16F	06:08:54.32	21:38:28.66	···	···	540	3	91	14
K16G	06:08:54.33	21:38:28.55	···	20	···	3	92	14
K16H	06:08:54.34	21:38:30.01	···	···	540	3	86	14
K16I	06:08:54.37	21:38:29.99	···	25	···	3	86	15
K16J	06:08:54.37	21:38:29.29	···	25	···	3	89	15
K16K	06:08:54.40	21:38:30.66	···	15	···	3	83	15
K16L	06:08:54.45	21:38:31.01	···	15	···	3	83	16
K16M	06:08:54.46	21:38:30.74	···	20	···	3	84	16
K17A	06:08:54.26	21:38:35.37	11	9	···	M | 13 | 14	64 | 72 | 63	14 | 4 | 2
K17B	06:08:54.28	21:38:35.43	···	7	···	M | 13 | 14	64 | 73 | 65	15 | 4 | 2
K18	06:08:54.55	21:38:28.21	15	5	85	3	92	17
K19A	06:08:56.54	21:38:05.02	5	–	···	M | S	118 | 96	51 | 47
K19B	06:08:56.66	21:38:01.38	9	–	···	M | S	121 | 100	54 | 49
K19C	06:08:56.75	21:38:00.71	15	–	···	M | S	121 | 101	55 | 50
K20	06:08:57.61	21:39:51.75	5	–	–	M | 13 | 14	36 | 33 | 32	102 | 92 | 91
K21	06:09:01.03	21:37:42.79	9	–	–	M | S	113 | 104	117 | 112

Table 2: Jet knots in AFGL 5180

A major open question in massive star formation concerns the importance of interactions between high-mass protostars and their lower-mass counterparts during the formation process. As discussed in Sect. 1, there are two main massive star formation models under active investigation: core accretion (e.g., McKee & Tan 2003) and competitive accretion (e.g., Bonnell et al. 2001;

Wang et al. 2010; Grudic et al. 2022). A major difference between these models is that competitive accretion predicts that high-mass stars necessarily form surrounded by a concentrated cluster of lower-mass YSOs. On the other hand, core accretion models do not require such a condition, i.e., massive star formation can occur in both isolated and clustered environments. Therefore, observational studies such as this one can place key constraints on massive star formation theories, through direct measurement of the distribution of YSOs (both in NIR LBT AO and ALMA) around high-mass protostars.

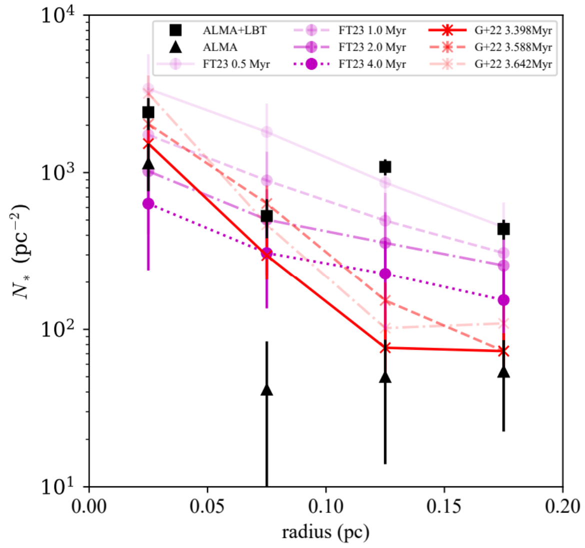

Figure 6: YSO number surface denstity analysis in AFGL 5180

The radial profile of YSO surface number density is shown in Fig. 6, evaluated in annuli of width 0.05 pc around the central massive protostar S4. The surface number density was derived by counting the number of YSO candidates within a given annulus. Note that most of the annuli have only partial coverage with the AO FOV, so their N∗ measurement is based only on the area that is covered by this FOV. This is compared to two recent star formation simulations, STARFORGE (Guszejnov et al. 2022; representing Competitive Accretion) and the protocluster N-body simulations from Farias & Tan (2023), representing Core Accretion.

4. Conclusions

In this paper, we have presented high-resolution NIR data towards the massive star-forming region AFGL 5180, which reveals the presence of ~40 outflow knots and a similar number of YSO candidates. With additional analysis of archival ALMA Band 6 and Band 7 data, we determine the locations of several protostellar YSO candidates. We have carried out an analysis to attempt to match outflow knots to driving sources. We conclude that a significant part of the outflow activity can be associated with a E–W bipolar outflow from the primary massive protostar in AFGL 5180, with many prominent knots in the east detected in both HST [FeII] and high-resolution LUCI-1 SOUL AO H2 observations. The massive protostar, which we identify as the S4 mm source, is estimated to have a current protostellar mass of ~11 M⊙ from SED fitting. In addition to the primary massive protostar, there are several other protostellar sources in the region, especially from AFGL 5180 S, that appear to be driving independent outflows in a variety of directions. From our census of YSOs, we have derived the YSO surface number density, N∗, i.e., by combining the ALMA-detected mm sources with the NIR K-band detected sources. The overall projected number densities inside 0.1 pc are consistent with models of both competitive accretion and core accretion (in the latter case with random sampling of cores or stars from a turbulent clump with an assumed power law density profile). The shape of the observed N∗(r) profile is a good match to the competitive accretion model inside 0.1 pc, but is shallower on larger scales, where it is a better match to the core accretion from Turbulent Clump model. Additional follow-up observations are needed to confirm the protostellar nature of the ALMA-detected sources in the inner 0.05 pc to better test predictions of these models.

References

Astropy Collaboration (Price-Whelan, A. M., et al.) 2022, ApJ, 935, 167

Bonnell, I. A., Bate, M. R., Clarke, C. J., & Pringle, J. E. 2001, MNRAS, 323, 785

Bradley, L. 2023, https://doi.org/10.5281/zenodo.7946442

CASA Team (Bean, B., et al.) 2022, PASP, 134, 114501

Craig, M., Crawford, S., Seifert, M., et al. 2022, https://doi.org/10.5281/zenodo.6533213

Davis, C. J., Moriarty-Schieven, G., Eislöffel, J., Hoare, M. G., & Ray, T. P. 1998, AJ, 115, 1118

Farias, J. P., & Tan, J. C. 2023, MNRAS, 523, 2083

Fedriani, R., Caratti o Garatti, A., Cesaroni, R., et al. 2023a, A&A, 676, A107

Gaia Collaboration (Vallenari, A., et al.) 2023, A&A, 674, A1

Grudic, M. Y., Guszejnov, D., Offner, S. S. R., et al. 2022, MNRAS, 512, 216

Guszejnov, D., Grudic, M. Y., Offner, S. S. R., et al. 2022, ´ MNRAS, 515, 4929

Hodapp, K.-W. 1994, ApJS, 94, 615

Longmore, S. N., Burton, M. G., Minier, V., & Walsh, A. J. 2006, MNRAS, 369, 1196

McKee, C. F., & Tan, J. C. 2003, ApJ, 585, 850

Mutie, M. M., Chibueze, J. O., El Bouchefry, K., et al. 2021, MNRAS, 506, 4175

Pinna, E., Esposito, S., Hinz, P., et al. 2016, SPIE Conf. Ser., 9909, 99093V

Seifert, W., Appenzeller, I., Baumeister, H., et al. 2003, SPIE Conf. Ser., 4841, 962

Snell, R. L., Huang, Y. L., Dickman, R. L., & Claussen, M. J. 1988, ApJ, 325, 853

Stetson, P. B. 1987, PASP, 99, 191

Tamura, M., Gatley, I., Joyce, R. R., et al. 1991, ApJ, 378, 611

Tan, J. C., Beltrán, M. T., Caselli, P., et al. 2014, in Protostars and Planets VI, eds. H. Beuther, R. S. Klessen, C. P. Dullemond, & T. Henning (Tucson: University of Arizona Press), 149

Tofani, G., Felli, M., Taylor, G. B., & Hunter, T. R. 1995, A&AS, 112, 299

Wang, P., Li, Z.-Y., Abel, T., & Nakamura, F. 2010, ApJ, 709, 27

Yao, Y., Ishii, M., Nagata, T., Nakaya, H., & Sato, S. 2000, ApJ, 542, 392